DOI: https://doi.org/10.2138/am-2024-9305. http://www.minsocam.org/

Word Count: 8333

Revision 1

Thermoelasticity of phase D and implications for low-velocity anomalies and local discontinuities at the uppermost lower mantle

Shangqin Hao[1,2], Dapeng Yang[1,3], Wenzhong Wang[1,3], Fan Zou[1], Zhongqing Wu[1,3,4*]

[1]*Laboratory of Seismology and Physics of Earth's Interior, School of Earth and Space Sciences, University of Science and Technology of China, Hefei, China*

[2]*Now at Institute of Geophysics and Planetary Physics, Scripps Institution of Oceanography, University of California San Diego, La Jolla, CA, USA*

[3]*National Geophysical Observatory at Mengcheng, University of Science and Technology of China, Hefei, China*

[4]*CAS Center for Excellence in Comparative Planetology, University of Science and Technology of China, China*

[*] Correspondences and requests for materials should be addressed to Zhongqing Wu (wuzq10@ustc.edu.cn)

Abstract

The distribution of water reservoirs in the deep Earth is critical to understanding geochemical evolution and mantle dynamics. Phase D is a potential water carrier in the slab subducted to the uppermost lower mantle (ULM) and its seismic velocity and density characteristics are important for seismological detection on water reservoirs, but these properties remain poorly constrained. Here we calculate the seismic velocities and density of Mg-endmember phase D ($MgSi_2H_2O_6$) under the ULM conditions using first-principles calculations based on the density functional theory. The velocities of phase D are higher than those of periclase and slightly lower than those of bridgmanite by 0.5–3.4% for V_P and by 0–1.9% for V_S between 660- and 1000-km depths. Considering its relatively low content, phase D can hardly produce a low-velocity anomaly in the ULM observed by seismological studies. However, due to its strong elastic anisotropy, it may contribute significantly to the observed seismic anisotropy at a similar depth. Additionally, phase D dehydrates into bridgmanite and stishovite at the ULM, producing insignificant velocity changes but a substantial density increase of ~14%. Therefore, the dehydration is probably too weak to generate discontinuities associated with velocity jumps, whereas it may account for seismic discontinuities that are sensitive to impedance changes, and particularly density jumps, near the dehydration depth observed in some subduction zones.

Keywords: Phase D, dense hydrous magnesium silicate, high-pressure phase transition, dehydration, impedance jump, seismic discontinuity

DOI: https://doi.org/10.2138/am-2024-9305. http://www.minsocam.org/

1. Introduction

Water in the Earth's interior exerts significant influences on geochemical evolution and mantle dynamics because a small amount of water can significantly change the rheological properties, melting temperature, diffusion rate of materials, and phase stability (Hirschmann, 2006; Karato and Jung, 2010; Mei and Kohlstedt, 2000). For example, water can reduce both viscosity and solidus temperature of mantle rocks, which significantly influences the pattern and velocity of mantle flow. It has been shown that wadsleyite and ringwoodite, candidate nominally anhydrous minerals in the mantle transition zone (MTZ), could incorporate several weight percent of H_2O (Bell and Rossman, 1992; Inoue et al., 2010; Inoue et al., 1995; Jacobsen et al., 2005; Smyth, 1987), whilst the hydrous ringwoodite and ice-VII discovered in superdeep diamonds (Pearson et al., 2014; Tschauner et al., 2018) provide direct evidence for the existence of the non-negligible amount of H_2O in the deep mantle. Water can be likely transported into the MTZ and the lower mantle via subducting slabs through the formation and dehydration of dense hydrous magnesium silicates (DHMSs) (Angel et al., 2001). Some geophysical anomalies, such as high V_P/V_S, high electrical conductivity, and low-velocity anomalies, were interpreted as locally high water content released by the dehydration of DHMSs (Karato, 2011; Li et al., 2013; Savage, 2012) or merely their existence owing to their low-velocity characteristics (Liu et al., 2016; Schmandt et al., 2014; Yang et al., 2017). Meanwhile, the generation/breakdown of DHMSs could also cause considerable impedance contrasts, giving rise to seismic discontinuities. For example, the decomposition of a small amount of superhydrous phase B may contribute to the 800-km discontinuity in western Pacific subduction zones (Yang et al., 2017), and the dehydration of phase H could produce significant seismic impedance increase in the mid-mantle (Song et al., 2022). Combining these seismological observations with the velocity and density characteristics, phase transitions, and corresponding impedance contrasts of DHMSs could help constrain the water content in the deep interior and provide insights into the circulation of water in the whole Earth.

Phase D is considered as a significant carrier of water in slabs subducted to the uppermost lower mantle (ULM). The ideal chemical formula of phase D is $MgSi_2H_2O_6$ containing 10 wt.% water, whereas the synthesized phase D shows a wide variation in Mg/Si ratio from 0.53 to 0.71 and the water content varies from 10 wt.% to 18 wt.% (Chang et al., 2013; Frost and Fei, 1999; Hushur et al., 2011; Litasov et al., 2007; Rosa et al., 2013a; Rosa et al., 2012; Shinmei et al., 2008; Wu et al., 2016; Xu et al., 2020; Xu et al., 2021b; Yang et al., 1997). Many hydrous phases exhibit low velocities (Li et al., 2016; Mao et al., 2012; Rosa et al., 2012; Rosa et al., 2015; Yang et al., 2017) and could be identified by seismic observations. The weight fraction of phase D can be as high as 57% in hydrous peridotite (Ohtani et al., 2004), which is also possible to generate seismic velocity anomalies in the MTZ and the ULM. On the other hand, phase D will dehydrate into bridgmanite and stishovite at low temperatures at the ULM (Nishi et al., 2014). Correspondingly, many seismic studies detected discontinuities exhibiting large impedance contrasts at the ULM in subduction zones (Courtier and Revenaugh, 2008; Schumacher and Thomas, 2016;

Waszek et al., 2018). The overlap of these depths may suggest a connection between these discontinuities and the dehydration of phase D. However, the velocities and density of phase D under the lower mantle conditions, which are crucial for deciphering its role in such seismic observations, remain unknown.

The crystal structure and equation of state of phase D have been widely studied (Frost and Fei, 1998; Frost and Fei, 1999; Hushur et al., 2011; Kudoh et al., 1997; Litasov et al., 2007; Liu, 1987; Liu et al., 1998; Rosa et al., 2013a; Rosa et al., 2012; Shieh et al., 2009; Shinmei et al., 2008; Wu et al., 2016; Xue et al., 2008; Yang et al., 1997) and the elastic properties of Mg-endmember phase D were investigated by first-principles calculations at static conditions (Mainprice et al., 2007; Thompson et al., 2022; Tsuchiya and Tsuchiya, 2008) and Brillouin scattering and ultrasonic measurements at ambient conditions (Liu et al., 2004; Rosa et al., 2012; Xu et al., 2021b). The sound velocities of Al-bearing phase D up to 22 GPa and 1300 K were also determined by ultrasonic measurements (Xu et al., 2020). However, there are no elasticity data of Mg-endmember phase D under both high-temperature and high-pressure conditions, which are crucial to understanding its characteristics and constraining its distribution. In this contribution, we obtained the elastic properties of Mg-endmember phase D ($MgSi_2H_2O_6$) and its velocity and density characteristics under the lower mantle conditions using first-principles calculations within the generalized gradient approximation. Combining our results with available data of other minerals, we calculated the velocity and impedance contrasts caused by its dehydration and discussed its close relationship to seismic observations in the ULM.

2. Computational Detail

The Mg-endmember phase D ($MgSi_2H_2O_6$) is trigonal and in the $P\bar{3}1m$ space group, with MgO_6 and SiO_6 octahedra in two separate layers stacked along the c-axis (Figure 1). The H–O bonds of phase D are located between adjacent octahedra in the MgO_6 layer and the hydrogens are only 1/3 occupied (Xue et al., 2008; Yang et al., 1997). To maintain the symmetries of phase D and handle the fractional occupancy of H atoms, instead of using a triclinic unit cell as the one in Tsuchiya et al. (2005), we constructed a super cell following Mainprice et al. (2007) (Figure 1). The basic vector (**a**, **b**, **c**) in this super cell is equal to (**a-b**, **a+2b**, **c)** in the unit cell, so it consists of 3 unit cells (33 atoms) and has a slightly different space group, $P\bar{3}m1$.

All calculations in this study were performed based on the density functional theory (DFT) using the open-source quantum espresso package (Giannozzi et al., 2009) with the Generalized Gradient Approximation (GGA) (Hamann, 1997; Perdew et al., 1996). The energy cutoff for the plane wave was set to 70 Ry. Structural optimizations were performed using the variable cell-shape damped molecular dynamics method (Wentzcovitch et al., 1993) at certain pressures with a k-point mesh of 6×6×6.

Isothermal elastic constants can be expressed as (Barron and Klein, 1965)

$$c_{ijkl}^{T} = \frac{1}{V}\left(\frac{\partial^2 F}{\partial e_{ij}\partial e_{kl}}\right) + \frac{1}{2}P\left(2\delta_{ij}\delta_{kl} - \delta_{il}\delta_{kj} - \delta_{ik}\delta_{jl}\right) , \quad (1)$$

where V , T , P , e_{ij} , δ_{ij} , and F represent the volume, temperature, pressure, infinitesimal strain, Kronecker delta, and Helmholtz free energy, respectively. Adiabatic elastic constants can be further calculated by

$$c_{ijkl}^{S} = c_{ijkl}^{T} + \frac{T}{VC_V}\frac{\partial S}{\partial e_{ij}}\frac{\partial S}{\partial e_{kl}}\delta_{ij}\delta_{kl} \ , \qquad (2)$$

where S and C_V represent the entropy and isochoric heat capacity, respectively. According to equation (1), Helmholtz free energy F is required to obtain these elastic constants, which, in quasi-harmonic approximation, is expressed as

$$F(V,T,e_{ij}) = U_0(V,e_{ij}) + \sum_{q,m}\frac{\hbar\omega_{qm}(V,e_{ij})}{2} + k_B T\sum_{q,m}\ln\{1-\exp[-\frac{\hbar\omega_{qm}(V,e_{ij})}{k_B T}]\}. \qquad (3)$$

The three terms on the right side are static internal, zero point, and vibrational energy, where $k_B$and $\hbar$ are Boltzmann and reduced Planck constants, respectively, and ω_{qm} is the vibrational frequency. Equation (1) and (3) suggest that the determination of all elastic constants requires the computation of vibrational frequencies, ω_{qm}, for many (~10) strained configurations, which is computationally demanding. To address this challenge, we employ the semi-analytical method developed by Wu and Wentzcovitch (2011) to calculate the thermal elasticity of phase D, which requires only the computation of vibrational frequencies under the unstrained condition and static elastic constants. The static elastic constants were calculated according to the stress-strain relationship with ±1% strain. The dynamical matrices with a 4×4×4 q-point mesh were calculated using density functional perturbation theory (Baroni et al., 2001) and further interpolated in a denser mesh to obtain the vibrational density of state. This method accelerates the computational efficiency by approximately tenfold while maintaining high accuracy, and it has been successfully applied to numerous minerals (Hao et al., 2019; Qian et al., 2018; Wang et al., 2020; Wang et al., 2019; Wu and Wang, 2016; Yang et al., 2017; Yao et al., 2018; Zou et al., 2018). At each pressure, we calculate the volume and corresponding vibrational frequencies under the unstrained condition, which are utilized to compute the Helmholtz free energy at different temperatures and volumes based on Equation (3). Finally, we apply the semi-analytical method developed by Wu and Wentzcovitch (2011) to calculate the adiabatic elastic constants.

3. Results

3.1 Absent H-bond symmetrization in optimized structures

Previous theoretical studies (Thompson et al., 2022; Tsuchiya and Tsuchiya, 2008; Tsuchiya et al., 2005) predicted that the hydrogen bond symmetrization (HBS) (the H atom is located at the middle point of two neighboring O atoms) takes place in phase D at the pressure of approximately 40 GPa, causing a ~20% increase in the bulk modulus. However, HBS is absent in the optimized structures up to 80 GPa in both Mainprice et al. (2007) and our study (Figure 1c) and neither of the studies shows an abrupt increase in the bulk modulus (see Section 3.3). The discrepancy is probably caused by different structural models of phase D related to the fractional occupancy of hydrogen, as discussed in Tsuchiya and Tsuchiya (2008). The structures of Mg-endmember phase D in their studies are unit cells, where H atoms occupy 2 of 6 sites, thus the structure distorts from trigonal and has a triclinic unit cell, whereas we use a triple cell to keep the symmetry.

Despite this discrepancy, infrared spectroscopic studies on phase D ($Mg_{2.23}Si_{1.18}H_{2.80}O_6$) observe neither significant changes in the frequency or intensity of OH stretching vibrations nor the merging of the separate OH peaks with increasing pressure up to 42 GPa (Shieh et al., 2009). In a recent study, Meier et al. (2022) suggest that the minima in the pressure dependence of the NMR resonance line-widths of Al- and Fe-bearing phase D ($(Mg_{0.88},Fe_{0.12})(Si_{0.9},Al_{0.1})O_6H_2$), which represents the maximum in hydrogen mobility, can be regarded as the precursor to HBS. However, based on first principles calculations, Thompson et al. (2022) suggest that phase D with 50% Al-substitution ($AlMg_{0.5}Si_{1.5}O_6H_2$), containing 8 unit cells in their setting, does not show HBS in the pressure range of 0–75 GPa, whereas both Mg- and Al-endmember phase D, containing one and two unit cells respectively, undergo pressure-induced HBS. The discrepancy in experiments and calculations suggests that whether HBS is present could be affected by both the structural models and compositions of phase D. Our results provide the optimized structures of Mg-endmember phase D based on the super-cell configuration and corresponding elastic properties at high temperatures, which can be combined with prior results to explore the effect of cell setting and Al content on the elasticity of phase D.

3.2 Thermodynamic Properties

The calculated equations of state of phase D are shown together with the experimental results in Figure 2. The differences among experiments primarily result from the wide variations in Mg/Si ratio, aluminum and water contents in the synthesized phase D. Except the Al-bearing phase D (Xu et al., 2020), most measured volumes (Frost and Fei, 1999; Hushur et al., 2011; Ohtani et al., 2004; Rosa et al., 2013a; Rosa et al., 2012; Rosa et al., 2013b; Shinmei et al., 2008; Wu et al., 2016; Xu et al., 2021b; Yang et al., 2017) are slightly smaller than our calculated results due to the overestimation of GGA calculation, but there is much better consistency in the relative change of volume (V/V_0) with pressure (Figure 2c). Our calculated volumes lie between the experimental data of Shinmei et al. (2008) and Wu et al. (2016) within a broad pressure range and agree with those of Rosa et al. (2013a) at all pressures (Figure 2c). Furthermore, the calculated relative changes in cell parameters are also consistent with the experimental results. In comparison with the absolute values at different pressures, the relative changes in volume (V/V_0) and lattice constants (a/a_0, c/c_0) play a more important role in the determination of the compressional properties.

The calculated thermal expansion ($\alpha = \frac{1}{V}\frac{\partial V}{\partial T}$) of phase D as well as the experimental data (Shinmei et al., 2008) are shown in Figure 3a. The blue dashed line represents the experimental results at 0 GPa (Shinmei et al., 2008), which are larger than our calculated results. The thermal expansion of Shinmei et al. (2008) was calculated using high-temperature Birch-Murnaghan equation of state (HTBM EOS) based on the P-V-T data of phase D. It should be noted that there are only two room-temperature volume data points at ambient pressure in their study, whereas most of the data were measured at 17-46 GPa. Therefore, the thermal expansion of phase D at high pressures should be more convincing than that at 0 GPa, and these high-pressure data do agree better with our calculated results (Figure 3a). The calculated thermal Grüneisen parameter, $\gamma_{th} = V\left(\frac{\partial P}{\partial U}\right)_V$ (U is the internal energy), decreases with pressure (Figure 3b). The heat capacity at constant volume ($C_V = \left(\frac{\partial U}{\partial T}\right)_V$) and constant pressure ($C_P = \left(\frac{\partial H}{\partial T}\right)_P$) (H is the enthalpy) increase significantly with temperature but slightly decreases with pressure (Figure 3c-d).

3.3 Thermal Elastic Properties

The elastic tensor of phase D with a trigonal symmetry can be totally determined by six independent elastic constants (C_{11}, C_{33}, C_{12}, C_{13}, C_{44}, and C_{14}). The calculated thermal elastic constants, adiabatic bulk (K_S) and shear (G) moduli, longitudinal (V_P) and shear wave (V_S) velocities as well as the experimental data (Rosa et al., 2012; Xu et al., 2020; Xu et al., 2021b) are shown in Figure 4. The first and second derivatives of elastic moduli M (M=C_{ij}, K_S, and G) with respect to pressure and temperature are shown in Table S1 and Table S2, respectively. The calculated compressional elastic constants (C_{11} and C_{33}) and shear elastic constant (C_{44}) are slightly larger than the experimental results (Rosa et al., 2012), whereas the off-diagonal elastic constants (C_{12}, C_{13}, and C_{14}) are slightly smaller (Figure 4). Since there are no high-pressure experimental data of elastic constants of phase D, we compared the linear compressibility calculated from our elastic constants with that from the lattice constants of experimental data and they exhibit good consistency (Text S1; Figure S1).

The adiabatic bulk moduli (K_S) are in good agreement with the experimental results of Rosa et al. (2012) and slightly larger than that of Xu et al. (2020) and Xu et al. (2021b), but our shear moduli (G) are significantly larger than all experiments, particularly Xu et al. (2021b) (Figure 4c). The deviations probably result from different Al and H_2O contents in phase D. Phase D in this study contains 10 wt.%

H_2O, whereas the synthesized samples in Rosa et al. (2012) and Xu et al. (2021b) include 12.1 and 16.1 wt.% H_2O, respectively, and the sample in Xu et al. (2020) contains 18.8 wt.% Al_2O_3 and ~16.0 wt.% H_2O. The negative correlation between the H_2O content and elastic moduli is consistent with many minerals, such as wadsleyite and ringwoodite (Wang et al., 2020; Wang et al., 2019), but the effect of aluminum content on the elastic moduli of phase D requires further investigation. Since the density of phase D in this study is close to these experiments and the compressional and shear wave velocities are expressed by $V_P = \sqrt{\left(K_S + \frac{4}{3}G\right)/\rho}$ and $V_S = \sqrt{G/\rho}$, the larger shear moduli further lead to higher velocities (Figure 4d). The V_P and V_S of phase D in this study are 3.0% and 5.8% larger than those in Rosa et al. (2012) at ambient conditions and approximately 4–6% and 8–9% larger than that in Xu et al. (2021b) at pressures of 3-13.6 GPa, respectively.

Our results do not show the abrupt increase in the bulk modulus of phase D up to 80 GPa, which disagrees with the result of Tsuchiya et al. (2005). They attribute the jump of bulk modulus to HBS at approximately 40 GPa, whereas the absent HBS in this study, which are probably caused by different cell settings as discussed in Section 3.1, does not cause such a jump. Among experimental results, the dramatic increase in bulk modulus observed by Hushur et al. (2011) probably results from the assumption of a fixed K_0' (the pressure derivative of the bulk modulus at 0 GPa) of 4, whereas Rosa et al. (2012), Xu et al. (2020) and this study obtain a value close to or larger than 5 (Table S1). The large K_0' can fit the equation of states well without an abrupt increase in bulk modulus.

3.4 Anisotropy

The elastic wave velocities of single crystal usually exhibit variations along different crystallographic orientations and the single-crystal anisotropy can be defined as in Karki et al. (2001):

$$A_P = 2 \times \frac{(V_{\mathrm{P,max}} - V_{\mathrm{P,min}})}{(V_{\mathrm{P,max}} + V_{\mathrm{P,min}})}$$
$$A_S = 2 \times \frac{(V_{\mathrm{S,max}} - V_{\mathrm{S,min}})}{(V_{\mathrm{S,max}} + V_{\mathrm{S,min}})} \qquad (4)$$
$$A_S^{Po} = 2 \times \frac{(V_{\mathrm{S1}} - V_{\mathrm{S2}})_{\mathrm{max}}}{V_{\mathrm{S1}} + V_{\mathrm{S2}}},$$

where A_P , A_S and A_S^{Po} represent the V_P , V_S , and V_S polarization anisotropies, respectively. V_P , V_{S1} , and V_{S2} represent the wave velocities along a given crystallographic orientation, which can be calculated using the Christoffel equation (Musgrave, 1970):

$$\left|C_{ijkl} n_j n_l - \rho V^2 \delta_{ik}\right| = 0. \qquad (5)$$

Here C_{ijkl} refers to the fourth-ranked elastic tensor and the unit vector **n** ((n_1, n_2, n_3)) is the propagation direction of the elastic wave. V and ρ represent velocity and density, respectively.

The S wave polarization anisotropy of phase D is significantly large (approximately 18%) under the conditions of the MTZ and ULM (Figure 5). Rosa et al. (2013b) indicate that phase D exhibits a relatively low strength under uniaxial compression and tends to develop lattice preferred orientations under plastic flow. They also estimated that 16 vol.% of phase D in hydrous subducted peridotite could explain the shear wave splitting (0.9±0.3%) and the shear wave ray polarization geometry observed in a detached fragment of the Tonga slab below the transition zone

(Chen and Brudzinski, 2003). Our calculated anisotropies of phase D are as strong as those in Rosa et al. (2012) (Figure 5), further corroborating this interpretation.

4. Discussions

4.1 The Velocities and Density Characteristics of Phase D in the MTZ and ULM

Phase D is stable at the lowermost MTZ and the ULM at low temperatures (Nishi et al., 2014). The seismic velocities and density of phase D, ringwoodite, periclase, bridgmanite, and stishovite along a cold geotherm 500 K lower than the normal geotherm (Brown and Shankland, 1981) are shown in Figure 6. Similar to other hydrous phases, phase D has a significantly lower density than all other minerals, especially at the ULM. The density contrast between phase D and bridgmanite is as large as ~13%, thus it could contribute to the stagnation of slabs at the depth of ~600–1000 km (Fukao et al., 2009) to a large extent. The seismic velocities of phase D, however, surpass or are comparable to those of candidate minerals. Phase D shows relatively high velocities in the MTZ, and the velocities of phase D increase faster with pressure than those of candidate minerals in the MTZ and ULM (Figure 6) due to its large pressure derivatives of K_S and G (Table S1). Its V_P and V_S are 1.5–3.0% and 6.5–8.7% higher than those of ringwoodite at depths of 500–660 km, respectively. Although phase D exhibits significantly lower velocities than bridgmanite at ambient conditions as in Rosa et al. (2012), the velocity contrasts between phase D and bridgmanite are not prominent for both V_P (0.5%–3.4%) and V_S (0%–1.9%) within the depth range of 660–1000 km (Figure 6). Moreover, the velocities of phase D are larger than periclase in the same depth range (Figure 6). Stishovite, one of the dehydration products of phase D (Nishi et al., 2014) and an important component in the oceanic crust, has significantly high velocities in the MTZ (Karki et al., 2001; Yang and Wu, 2014; Zhang et al., 2021). The velocity contrasts between phase D and stishovite are 11.1–13.1% for V_P and 10.2–12.7% for V_S at depths of 500–660 km. However, due to the softening of shear modulus of stishovite (Karki et al., 2001; Yang and Wu, 2014; Zhang et al., 2021) and the large pressure dependence of velocities of phase D, the V_P and V_S of stishovite are only 5.6% and 1.6% higher than those of phase D at 1000-km depth, respectively, which become even smaller at larger depths (Figure 6).

The comparable velocities of phase D to candidate minerals in the ULM suggest that the accumulation of phase D can hardly produce prominent low-velocity anomalies in the ULM observed by some seismological studies (Brudzinski and Chen, 2003; Liu et al., 2016), which is inconsistent with the conclusion drawn at ambient conditions (Rosa et al., 2012). H_2O and Al have a significant effect on the velocities and density of phase D. The velocities of phase D are negatively correlated with the H_2O content (Figure 4), so a higher H_2O content may increase the possibility of generating low-velocity anomalies, but it still requires more quantitative investigations on the effect. Xu et al. (2020) used the data of Al-bearing phase D, which include 18.8 wt.% Al_2O_3 and ~16.0 wt.% H_2O, to calculate the velocities and density contrasts between the dry and hydrous harzburgite. Their calculation indicates that the hydrous harzburgite with ~1.2 wt.% H_2O exhibits slightly lower velocities at the ULM, -0.5% and -1.0% for V_P and V_S respectively, hardly accounting for the -3% velocity anomalies for both V_P and V_S in Tonga slab (Brudzinski and Chen, 2003), although their Al-bearing phase D has lower velocities than the Mg-endmember phase D in our study under such conditions. This calculation provides an approximate estimation on the H_2O effect, that is, such a water content is not enough to cause obvious low-velocity anomalies, but the contribution of Al to the velocities remains to be explored.

In contrast, superhydrous phase B, another stable hydrous mineral in cold slabs in the ULM, may explain these low-velocity observations. It has much lower velocities than bridgmanite and periclase, and the released water by its dehydration at the depth of ~800 km should migrate upwards, causing the partial melt to reduce the velocity at a shallower depth (Yang et al., 2017). However, superhydrous phase B has negligible anisotropy compared with the strong anisotropy of phase D (Figure 5) under such conditions, which cannot explain the observed seismic anisotropy in the same region (Chen and Brudzinski, 2003). Previous studies suggest that phase D and superhydrous phase B are likely to coexist in the ULM at low temperatures (Nishi et al., 2014; Xu et al., 2021a). Therefore, the low-velocity anomaly could be mainly caused by superhydrous phase B, whereas phase D may primarily contribute to the seismic anisotropy.

4.2 The Dehydration of Phase D and Implications on Discontinuities in the ULM

At the ULM, with increasing pressure and temperature, phase D should dehydrate into bridgmanite and stishovite:

$$\mathrm{MgSi_2O_6(phase\ D) = MgSiO_3(bridgmanite) + SiO_2(stishovite) + H_2O},$$

but the transition depth spans a wide range due to its significantly large negative Clapeyron slope (dP/dT) (Nishi et al., 2014). Assuming that the slab is around 400–500 K lower than the normal geotherm (Brown and Shankland, 1981), the dehydration could take place across a broad depth range of approximately 700–1000 km, with potential deviations influenced by uncertainties in the phase boundary (Nishi et al., 2014). The V_P, V_S, and density contrasts between phase D and the aggregate of bridgmanite plus stishovite along a cold isotherm 500 K lower than the normal geotherm are shown in Figure 7. It is expected that the velocity jumps caused by the dehydration of phase D decrease with increasing pressure because the velocities of phase D increase faster with pressure than those of bridgmanite and stishovite and the shear modulus of stishovite soften at high pressures (Karki et al., 2001; Yang and Wu, 2014; Zhang et al., 2021) (Figure 6). The velocity jumps caused by the dehydration of phase D are 5.8% for V_P and 4.4% for V_S at 700-km depth but reduce to 2.3% and 0.4% at 1000-km depth, respectively (Figure 7). At deeper depths, the dehydration of phase D even results in a decrease in V_S. In contrast, the density jump caused by the dehydration of phase D is as large as ~14% at the depth of ~700–1000 km. The impedance contrasts ($\Delta(\rho V)$, where ρ and V represent the density and wave velocity, respectively) caused by the dehydration of phase D are 20% and 16% for compressional wave and 19% and 14% for shear wave at 700- and 1000-km depths, respectively, which are comparable to the transformation from olivine to wadsleyite (Núñez Valdez et al., 2013) accounting for the 410-km discontinuity. Such large impedance contrasts indicate that a small amount of phase D could produce seismically detectable discontinuities at the ULM in subduction zones.

It should be noted that the effects of iron on the elasticity of phase D are not considered above. Previous studies indicate that the iron in Fe-Al-bearing phase D undergoes a high-spin to low-spin transition, which significantly reduce the bulk modulus of phase D (Chang et al., 2013; Wu et al., 2016). The pressure range of the spin transition in Fe-Al-bearing phase D is related to the valence state of iron. The spin transition of Fe^{2+} occurs at 37-41 GPa and the spin transition of Fe^{3+} occurs at 40-65 GPa for $\sum Fe^{3+}/Fe = 0.94$ and at 64-68 GPa for $\sum Fe^{3+}/Fe = 0.40$ (Chang et al., 2013; Wu et al., 2016). Therefore, the spin transition of Fe^{2+} in phase D and the dehydration of phase D are likely to occur simultaneously near the 1000-km depth if phase D contains a certain amount of Fe^{2+}. The spin transition of Fe^{2+} in phase D ($Mg_{0.89}Fe_{0.11}Al_{0.37}Si_{1.55}H_{2.65}O_6$ $\sum Fe^{2+}/Fe = 0.60$) will cause a reduction of 28% on bulk sound velocity and a reduction of 1.7% on volume (Wu et al., 2016). Iron in bridgmanite occupies mainly in the Mg site as Fe^{2+} or Fe^{3+}, and the iron does not experience any spin transition over the entire pressure range of the lower mantle. Si site in bridgmanite may contain a small amount of Fe^{3+}, and the Fe^{3+} undergoes a spin transition at approximately 15–50 GPa (Lin et al., 2013), whose effect on bulk modulus of bridgmanite is relatively small at relevant mantle conditions (Badro, 2014; Catalli et al., 2011; Catalli et al., 2010; Shukla and Wentzcovitch, 2016). Therefore, the spin transition of Fe^{2+} may significantly increase the V_P jump and slightly decrease the density jump caused by the dehydration of phase D at the depth of ~1000 km. Thus, the compressional impedance contrast caused by the dehydration of Fe-bearing phase D may significantly increase if the Fe^{2+} in phase D undergoes a spin transition.

Besides the global 410-km and 660-km discontinuities, seismological studies detected many local discontinuities in the ULM, especially in subduction zones, and their origins have been widely discussed (Courtier and Revenaugh, 2008; Schumacher and Thomas, 2016; Waszek et al., 2018). These detections are sensitive to the impedance contrasts across discontinuities and the most robust ones are at the depth of ~800 km and ~1000 km, respectively. The dehydration of superhydrous phase B may account for the discontinuities at the depth of ~800 km in subduction zones (Liu et al., 2016; Porritt and Yoshioka, 2016; Yang et al., 2017), but the ones at the depth of ~1000 km were ascribed to various mechanisms including viscosity jump (Marquardt and Miyagi, 2015; Rudolph et al., 2015), mineral phase transitions within subducted slab (King et al., 2015; Kingma et al., 1995), and the impedance contrasts between oceanic crust and other parts of a slab (Niu, 2014; Rost et al., 2008). The dehydration of phase D causes substantial impedance contrasts at the ULM, providing another mechanism for these discontinuities. Most of these discontinuities are roughly located within the fast anomalies in tomography models, that is, subducted slabs, where the dehydration of phase D takes place. The dehydration of phase D at the ULM mainly accounts for discontinuities caused by large impedance contrasts, specifically, density contrast. Therefore, seismic observations which are mainly sensitive to the velocity contrast, such as the S-to-P scatterers beneath the circum-Pacific regions near 1000-

DOI: https://doi.org/10.2138/am-2024-9305. http://www.minsocam.org/

km depth, may not result from the dehydration of phase D, where the presence of oceanic crust is more preferred (Kaneshima, 2019).

5. Implications

In this study, we obtain the elasticity of Mg-endmember phase D at high pressures and high temperatures using first-principles calculations based on the density functional theory with the generalized gradient approximation. Compared with other candidate minerals, the low-density feature of phase D could contribute to the stagnation of slabs at the ULM. On the other hand, phase D has larger pressure derivatives of K and G than those of major minerals in the MTZ and ULM, thus its velocities increase much faster with depth. As a result, unlike other hydrous phases, phase D exhibits higher velocities than ringwoodite at the transition zone and comparable velocities to bridgmanite, periclase, and stishovite in the ULM, respectively. Therefore, the accumulation of phase D is not likely to cause prominent low-velocity anomalies at the ULM. In contrast, superhydrous phase B, another hydrous phase coexisting with phase D at the ULM, may account for the low-velocity anomalies, whereas phase D could explain the shear wave splitting in the same region.

The velocity contrasts caused by the dehydration of phase D into stishovite and bridgmanite are negligible at the ULM, but the impedance contrasts are significantly large because of the large density jump (~14%). Such large impedance contrasts may provide an alternative explanation for the discontinuities at the ULM in subduction regions. The equation of states and elasticity of Mg-endmember phase D obtained in this study can be combined with other studies with different Al and water contents to explore the effect of composition on these physical properties.

Acknowledgements

This study is supported by the National Natural Science Foundation of China (41925017), and the Fundamental Research Funds for the Central Universities (WK2080000144). The calculations were conducted in the Supercomputing Center of the University of Science and Technology of China. The original data for all the figures are available at the Zenodo database (https://doi.org/10.5281/zenodo.10452880).

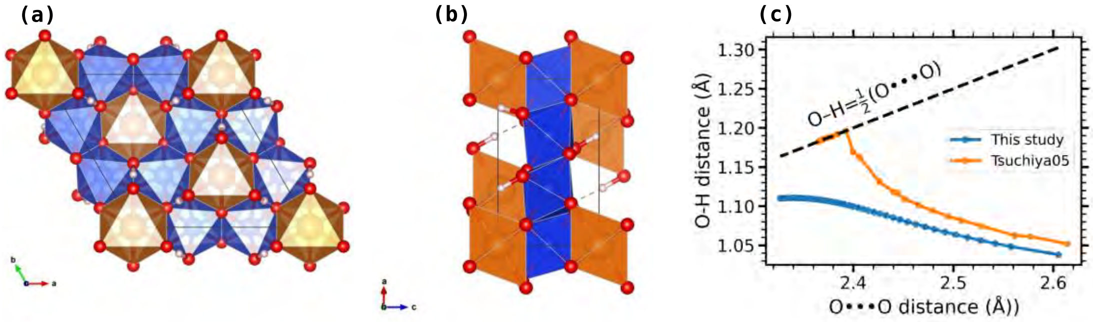

Figure 1. (a) (b) Crystal structure of phase D at 0 GPa. The yellow, blue, red, and white balls are Si, Mg, O, and H atoms, respectively. Images were generated in VESTA (Momma and Izumi, 2008). (c) The relationship between the O···O and the O–H distances of phase D in our study, shown in blue, and Tsuchiya et al. (2005), shown in orange. The dashed line represents the relationship of hydrogen bond symmetrization.

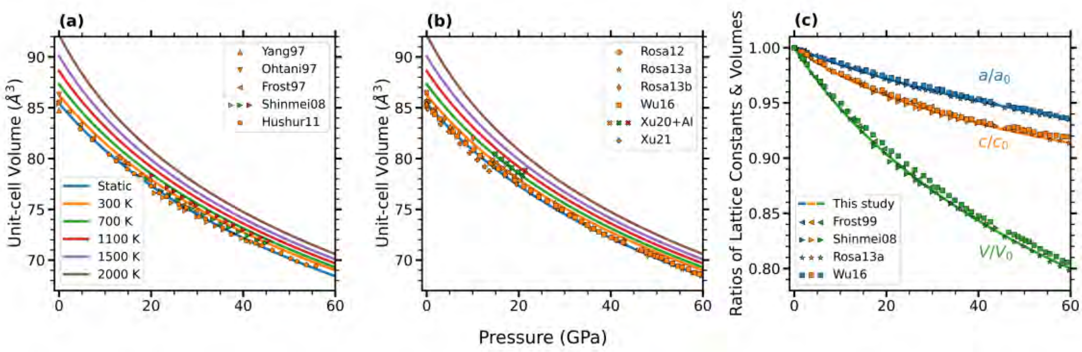

Figure 2. (a) The equation of states of phase D, (b) the relative change in volume (V/V_0), and (c) lattice constant (a/a_0, c/c_0) as a function of pressure (this study: static results; experiments: data at 300 K). Solid lines represent our calculation results and the experimental results are shown with scatters. Chemical formulas: $MgSi_2H_2O_6$ (this study), $Mg_{1.11}Si_{1.89}H_{2.22}O_6$ (Yang et al., 1997), $Mg_{1.14}Si_{1.73}H_{2.81}O_6$ (Ohtani et al., 1997), $Mg_{1.11}Si_{1.6}H_{3.6}O_6$ (Frost and Fei, 1999), $Mg_{1.02}Si_{1.73}H_{3.03}O_6$ (Shinmei et al., 2008), $Mg_{1.0}Si_{1.7}H_{3.0}O_6$ (Hushur et al., 2011), $Mg_{1.1}Si_{1.9}H_{2.4}O_6$ (Rosa et al., 2012), $Mg_{1.1}Si_{1.8}H_{2.5}O_6$ (Rosa et al., 2013a; Rosa et al., 2013b), $Mg_{1.14}Si_{1.73}H_{2.81}O_6$ (Wu et al., 2016), $Mg_{0.89}Si_{1.30}Al_{0.64}H3_{.10}O_6$ (Al-bearing phase D) (Xu et al., 2020), $Mg_{1.03}Si_{1.71}H_{3.05}O_6$ (Xu et al., 2021b).

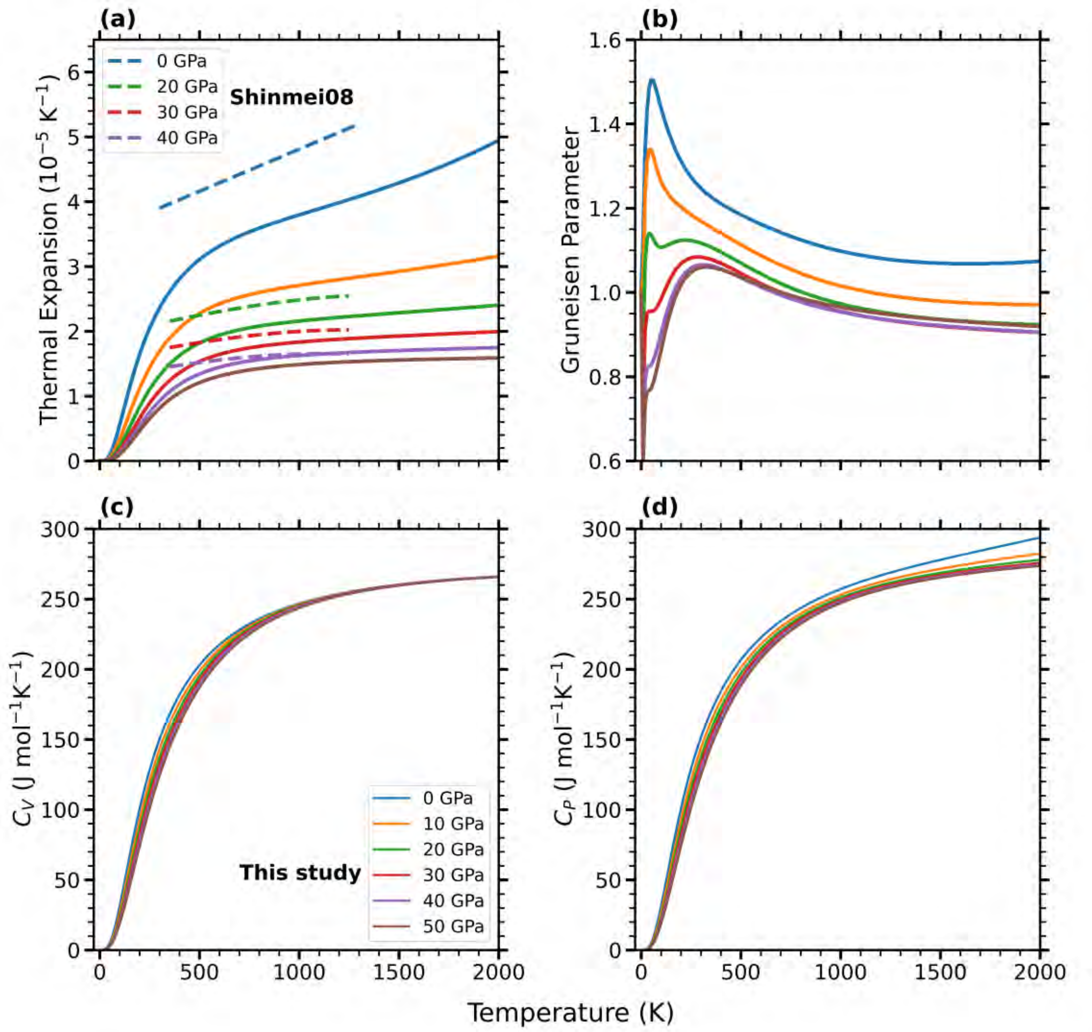

Figure 3. (a) thermal expansion, (b) thermal Grüneisen parameter, (c) heat capacity at constant volume, and (d) heat capacity at constant pressures of phase D. Solid lines represent our calculation results at various pressures and dashed lines represent the experimental results from HTBM EOS of phase D reported by Shinmei et al. (2008).

DOI: https://doi.org/10.2138/am-2024-9305. http://www.minsocam.org/

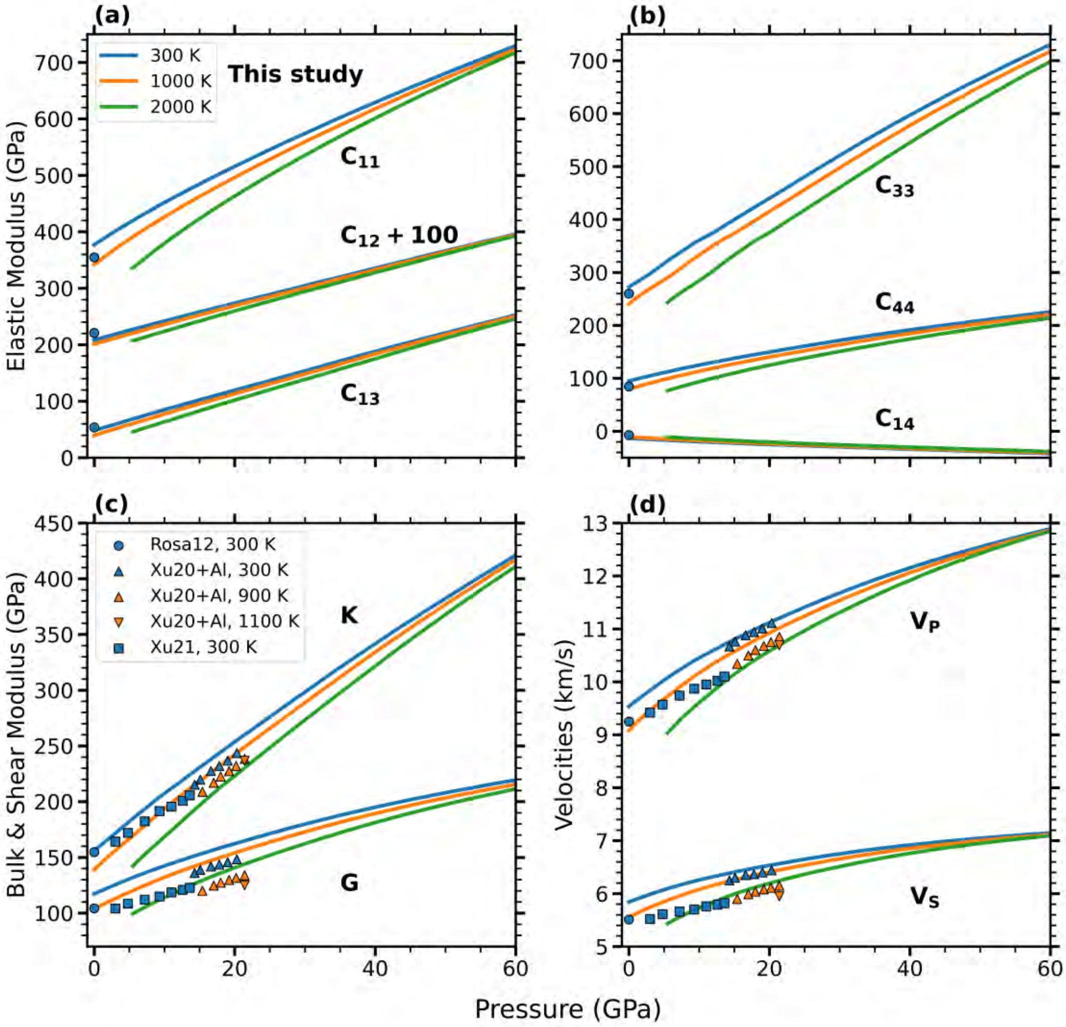

Figure 4. (a and b) elastic constants, (c) bulk modulus and shear modulus, (d) compressional wave velocity, and shear wave velocity of phase D at various pressures and temperatures. Solid lines represent our calculation results and the experimental results are shown with scatters. Chemical formulas: This study, $MgSi_2H_2O_6$; Rosa12, $Mg_{1.1}Si_{1.9}H_{2.4}O_6$ (Rosa et al., 2012); Xu20+Al, $Mg_{0.89}Si_{1.30}Al_{0.64}H_{3.10}O_6$ (Xu et al., 2020); Xu21, $Mg_{1.03}Si_{1.71}H_{3.05}O_6$ (Xu et al., 2021b).

DOI: https://doi.org/10.2138/am-2024-9305. http://www.minsocam.org/

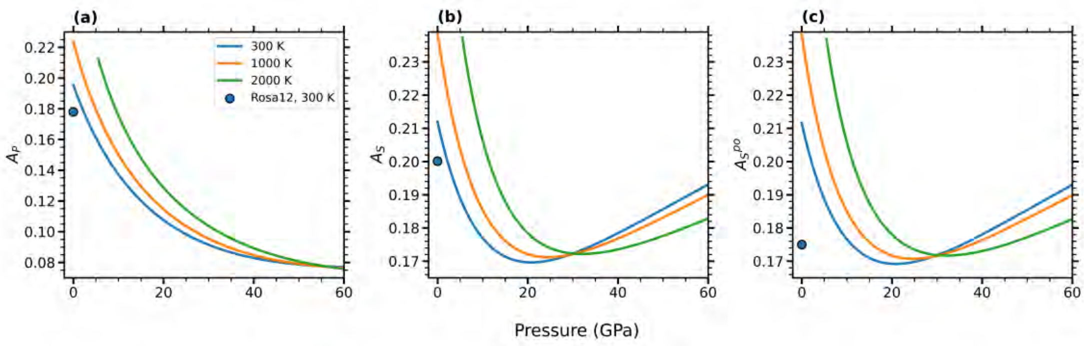

Figure 5. Anisotropy of phase D as a function of pressure. (a) A_P, (b) A_S, and (c) A_S^{po} of phase D at various pressures and temperatures. Blue circles represent the experimental results at ambient conditions obtained by Rosa et al. (2012).

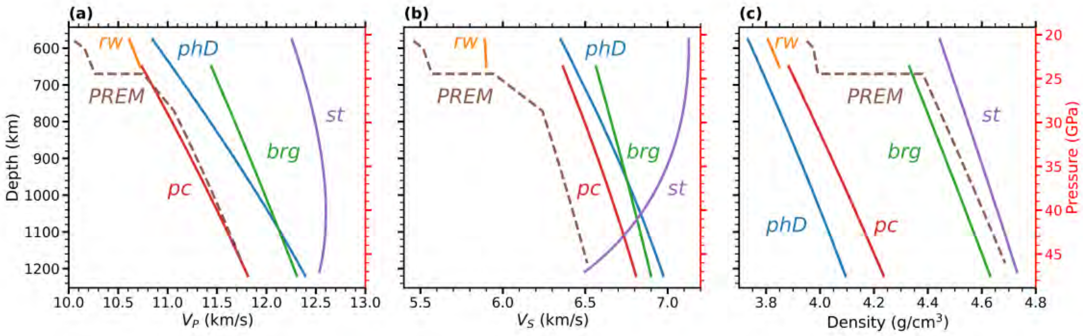

Figure 6. (a) Compressional wave velocity V_P, (b) shear wave velocity V_S, and (c) densities of phase D (phD) compared to those of iron-free ringwoodite (rw) (Núñez Valdez et al., 2012), stishovite (st) (Yang and Wu, 2014), iron-free bridgmanite (brg) (Shukla et al., 2015) and periclase (pc) (Wu and Wentzcovitch, 2011) along a slab geotherm 500 K lower than the normal mantle geotherm (Brown and Shankland, 1981). The dashed lines show the profiles of the 1D seismic reference model PREM (Dziewonski and Anderson, 1981).

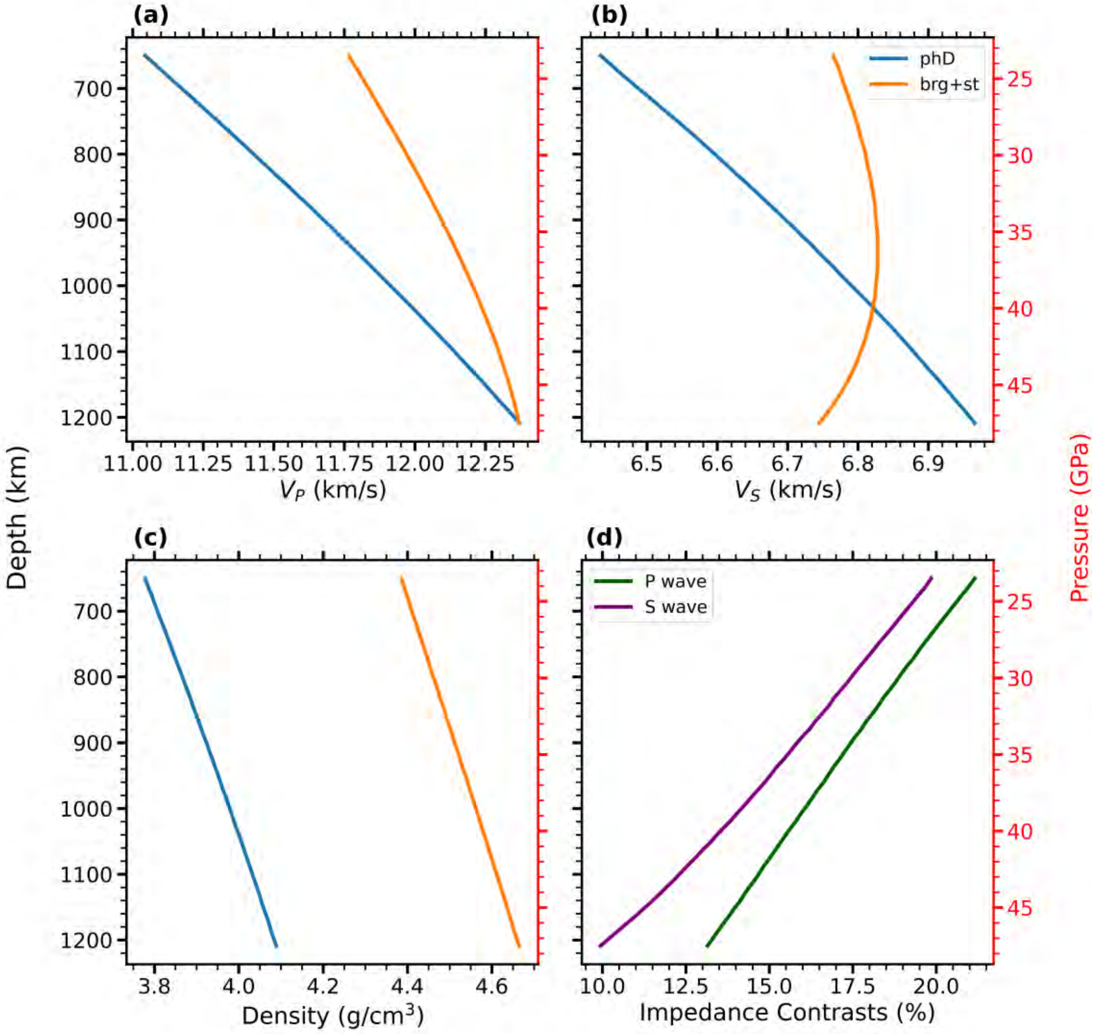

Figure 7. (a) Compressional wave velocity V_P, (b) shear wave velocity V_S, and (c) densities of phase D (phD) and the aggregate of bridgmanite (brg) (Shukla et al., 2015) and stishovite (st) (Yang and Wu, 2014) along the cold isotherm. (d) Impedance contrasts of P and S waves caused by the dehydration of phase D into bridgmanite and stishovite.

References

Angel, R.J., Frost, D.J., Ross, N.L., Hemley, R., 2001. Stabilities and equations of state of dense hydrous magnesium silicates. Phys Earth Planet In 127, 181-196.

Badro, J., 2014. Spin Transitions in Mantle Minerals. Annual Review of Earth and Planetary Sciences, Vol 42 42, 231-248.

Baroni, S., de Gironcoli, S., Dal Corso, A., Giannozzi, P., 2001. Phonons and related crystal properties from density-functional perturbation theory. Reviews of Modern Physics 73, 515-562.

Barron, T., Klein, M., 1965. Second-order elastic constants of a solid under stress. Proceedings of the Physical Society 85, 523.

Bell, D.R., Rossman, G.R., 1992. Water in Earths Mantle - the Role of Nominally Anhydrous Minerals. Science 255, 1391-1397.

Brown, J., Shankland, T., 1981. Thermodynamic parameters in the Earth as determined from seismic profiles. J Geophysical Journal International 66, 579-596.

Brudzinski, M.R., Chen, W.-P., 2003. A petrologic anomaly accompanying outboard earthquakes beneath Fiji-Tonga: Corresponding evidence from broadbandPandSwaveforms. Journal of Geophysical Research: Solid Earth 108.

Catalli, K., Shim, S.-H., Dera, P., Prakapenka, V.B., Zhao, J., Sturhahn, W., Chow, P., Xiao, Y., Cynn, H., Evans, W.J., 2011. Effects of the Fe^{3+} spin transition on the properties of aluminous perovskite—New insights for lower-mantle seismic heterogeneities. Earth Planet Sc Lett 310, 293-302.

Catalli, K., Shim, S.H., Prakapenka, V.B., Zhao, J.Y., Sturhahn, W., Chow, P., Xiao, Y.M., Liu, H.Z., Cynn, H., Evans, W.J., 2010. Spin state of ferric iron in $MgSiO_3$ perovskite and its effect on elastic properties. Earth Planet Sc Lett 289, 68-75.

Chang, Y.Y., Jacobsen, S.D., Lin, J.F., Bina, C.R., Thomas, S.M., Wu, J.J., Shen, G.Y., Xiao, Y.M., Chow, P., Frost, D.J., McCammon, C.A., Dera, P., 2013. Spin transition of Fe^{3+} in Al-bearing phase D: An alternative explanation for small-scale seismic scatterers in the mid-lower mantle. Earth Planet Sc Lett 382, 1-9.

Chen, W.P., Brudzinski, M.R., 2003. Seismic anisotropy in the mantle transition zone beneath Fiji-Tonga. Geophys Res Lett 30, 1682.

Courtier, A.M., Revenaugh, J., 2008. Slabs and shear wave reflectors in the midmantle. Journal of Geophysical Research: Solid Earth 113.

Dziewonski, A.M., Anderson, D.L., 1981. Preliminary reference Earth model. Phys Earth Planet In 25, 297-356.

Frost, D.J., Fei, Y., 1998. Stability of phase D at high pressure and high temperature. Journal of Geophysical Research: Solid Earth 103, 7463-7474.

Frost, D.J., Fei, Y., 1999. Static compression of the hydrous magnesium silicate phase D to 30 GPa at room temperature. Phys Chem Miner 26, 415-418.

Fukao, Y., Obayashi, M., Nakakuki, T., 2009. Stagnant Slab: A Review. Annual Review of Earth and Planetary Sciences 37, 19-46.

Giannozzi, P., Baroni, S., Bonini, N., Calandra, M., Car, R., Cavazzoni, C., Ceresoli, D., Chiarotti, G.L., Cococcioni, M., Dabo, I., Dal Corso, A., de Gironcoli, S., Fabris, S., Fratesi, G., Gebauer, R., Gerstmann, U., Gougoussis, C., Kokalj, A., Lazzeri, M., Martin-Samos, L., Marzari, N., Mauri, F., Mazzarello, R., Paolini, S., Pasquarello, A., Paulatto, L., Sbraccia, C., Scandolo, S., Sclauzero, G., Seitsonen, A.P., Smogunov, A., Umari, P., Wentzcovitch, R.M., 2009. QUANTUM ESPRESSO: a modular and open-source software project for quantum simulations of materials. J Phys Condens Matter 21, 395502.

Hamann, D.R., 1997. H_2O hydrogen bonding in density-functional theory. Phys Rev B 55, 10157-10160.

Hao, S., Wang, W., Qian, W., Wu, Z.J.E., Letters, P.S., 2019. Elasticity of akimotoite under the mantle conditions: Implications for multiple discontinuities and seismic anisotropies at the depth of∼ 600–750 km in subduction zones. 528, 115830.

Hirschmann, M.M., 2006. Water, melting, and the deep Earth H_2O cycle, Annual Review of Earth and Planetary Sciences. Annual Reviews, Palo Alto, pp. 629-653.

Hushur, A., Manghnani, M.H., Smyth, J.R., Williams, Q., Hellebrand, E., Lonappan, D., Ye, Y., Dera, P., Frost, D.J., 2011. Hydrogen bond symmetrization and equation of state of phase D. Journal of Geophysical Research-Solid Earth 116.

Inoue, T., Wada, T., Sasaki, R., Yurimoto, H.J.P.o.t.E., Interiors, P., 2010. Water partitioning in the Earth's mantle. 183, 245-251.

Inoue, T., Yurimoto, H., Kudoh, Y.J.G.R.L., 1995. Hydrous modified spinel, Mg1. 75SiH0. 5O4: a new water reservoir in the mantle transition region. 22, 117-120.

Jacobsen, S.D., Demouchy, S., Frost, D.J., Ballaran, T.B., Kung, J.J.A.M., 2005. A systematic study of OH in hydrous wadsleyite from polarized FTIR spectroscopy and single-crystal X-ray diffraction: Oxygen sites for hydrogen storage in Earth’s interior. 90, 61-70.

Kaneshima, S., 2019. Seismic scatterers in the lower mantle near subduction zones. Geophys J Int 219, S2-S20.

Karato, S.-i., 2011. Water distribution across the mantle transition zone and its implications for global material circulation. Earth Planet Sc Lett 301, 413-423.

Karato, S.-I., Jung, H., 2010. Effects of pressure on high-temperature dislocation creep in olivine. Philos Mag 83, 401-414.

Karki, B.B., Stixrude, L., Wentzcovitch, R.M., 2001. High-pressure elastic properties of major materials of Earth's mantle from first principles. Rev Geophys 39, 507-534.

King, S.D., Frost, D.J., Rubie, D.C.J.G., 2015. Why cold slabs stagnate in the transition zone. 43, 231-234.

Kingma, K.J., Cohen, R.E., Hemley, R.J., Mao, H.-k.J.N., 1995. Transformation of stishovite to a denser phase at lower-mantle pressures. 374, 243-245.

Kudoh, Y., Nagase, T., Mizohata, H., Ohtani, E., Sasaki, S., Tanaka, M., 1997. Structure and crystal chemistry of phase G, a new hydrous magnesium silicate synthesized at 22 GPa and 1050 degrees C. Geophys Res Lett 24, 1051-1054.

Li, J., Wang, X., Wang, X.J., Yuen, D.A., 2013. P and SH velocity structure in the upper mantle beneath Northeast China: Evidence for a stagnant slab in hydrous mantle transition zone. Earth Planet Sc Lett 367, 71-81.

Li, X.Y., Mao, Z., Sun, N.Y., Liao, Y.F., Zhai, S.M., Wang, Y., Ni, H.W., Wang, J.Y., Tkachev, S.N., Lin, J.F., 2016. Elasticity of single-crystal superhydrous phase B at simultaneous high pressure-temperature conditions. Geophys Res Lett 43, 8458-8465.

Lin, J.-F., Speziale, S., Mao, Z., Marquardt, H., 2013. Effects of the Electronic Spin Transitions of Iron in Lower Mantle Minerals: Implications for Deep Mantle Geophysics and Geochemistry. Rev Geophys 51, 244-275.

Litasov, K.D., Ohtani, E., Suzuki, A., Funakoshi, K., 2007. The compressibility of Fe- and Al-bearing phase D to 30 GPa. Phys Chem Miner 34, 159-167.

Liu, L.G., 1987. Effects of H_2O on the Phase-Behavior of the Forsterite Enstatite System at High-Pressures and Temperatures and Implications for the Earth. Phys Earth Planet In 49, 142-167.

Liu, L.G., Lin, C.C., Irifune, T., Mernagh, T.P., 1998. Raman study of phase D at various pressures and temperatures. Geophys Res Lett 25, 3453-3456.

Liu, L.G., Okamoto, K., Yang, Y.J., Chen, C.C., Lin, C.C., 2004. Elasticity of single-crystal phase D (a dense hydrous magnesium silicate) by Brillouin spectroscopy. Solid State Commun. 132, 517-520.

Liu, Z., Park, J., Karato, S.I., 2016. Seismological detection of low-velocity anomalies surrounding the mantle transition zone in Japan subduction zone. Geophys Res Lett 43, 2480-2487.

Mainprice, D., Le Page, Y., Rodgers, J., Jouanna, P., 2007. Predicted elastic properties of the hydrous D phase at mantle pressures: Implications for the anisotropy of subducted slabs near 670-km discontinuity and in the lower mantle. Earth Planet Sc Lett 259, 283-296.

Mao, Z., Lin, J.F., Jacobsen, S.D., Duffy, T.S., Chang, Y.Y., Smyth, J.R., Frost, D.J., Hauri, E.H., Prakapenka, V.B., 2012. Sound velocities of hydrous ringwoodite to 16GPa and 673K. Earth Planet Sc Lett 331-332, 112-119.

Marquardt, H., Miyagi, L.J.N.G., 2015. Slab stagnation in the shallow lower mantle linked to an increase in mantle viscosity. 8, 311-314.

Mei, S., Kohlstedt, D.L., 2000. Influence of water on plastic deformation of olivine aggregates 1. Diffusion creep regime. Journal of Geophysical Research-Solid Earth 105, 21457-21469.

Meier, T., Trybel, F., Khandarkhaeva, S., Laniel, D., Ishii, T., Aslandukova, A., Dubrovinskaia, N., Dubrovinsky, L., 2022. Structural independence of hydrogen-bond symmetrisation dynamics at extreme pressure conditions. Nat Commun 13, 3042.

Momma, K., Izumi, F., 2008. VESTA: a three-dimensional visualization system for electronic and structural analysis. Journal of Applied crystallography 41, 653-658.

Musgrave, M.J.P., 1970. Crystal Acoustics: Introduction to the Study of Elastic Waves and Vibrations in Crystals. Holden-Day, San Francisco, Calif.

Nishi, M., Irifune, T., Tsuchiya, J., Tange, Y., Nishihara, Y., Fujino, K., Higo, Y., 2014. Stability of hydrous silicate at high pressures and water transport to the deep lower mantle. Nature Geoscience 7, 224-227.

Niu, F., 2014. Distinct compositional thin layers at mid-mantle depths beneath northeast China revealed by the USArray. Earth Planet Sc Lett 402, 305-312.

Núñez Valdez, M., Wu, Z., Yu, Y.G., Wentzcovitch, R.M., 2013. Thermal elasticity of $(Fe_x,Mg_{1-x})_2SiO_4$ olivine and wadsleyite. Geophys Res Lett 40, 290-294.

Núñez Valdez, M., Wu, Z.Q., Yu, Y.G., Revenaugh, J., Wentzcovitch, R.M., 2012. Thermoelastic properties of ringwoodite $(Fe_x,Mg_{1-x})_2SiO_4$: Its relationship to the 520km seismic discontinuity. Earth Planet Sc Lett 351-352, 115-122.

Ohtani, E., Litasov, K., Hosoya, T., Kubo, T., Kondo, T., 2004. Water transport into the deep mantle and formation of a hydrous transition zone. Phys Earth Planet In 143, 255-269.

Ohtani, E., Mizobata, H., Kudoh, Y., Nagase, T., Arashi, H., Yurimoto, H., Miyagi, I., 1997. A new hydrous silicate, a water reservoir, in the upper part of the lower mantle. Geophys Res Lett 24, 1047-1050.

Pearson, D.G., Brenker, F.E., Nestola, F., McNeill, J., Nasdala, L., Hutchison, M.T., Matveev, S., Mather, K., Silversmit, G., Schmitz, S., Vekemans, B., Vincze, L., 2014. Hydrous mantle transition zone indicated by ringwoodite included within diamond. Nature 507, 221-224.

Perdew, J.P., Burke, K., Ernzerhof, M., 1996. Generalized Gradient Approximation Made Simple. Phys Rev Lett 77, 3865-3868.

Porritt, R.W., Yoshioka, S., 2016. Slab pileup in the mantle transition zone and the 30 May 2015 Chichi-jima earthquake. Geophys Res Lett 43, 4905-4912.

Qian, W.S., Wang, W.Z., Zou, F., Wu, Z.Q., 2018. Elasticity of Orthoenstatite at High Pressure and Temperature: Implications for the Origin of Low V_P/V_S Zones in the Mantle Wedge. Geophys Res Lett 45, 665-673.

Rosa, A.D., Mezouar, M., Garbarino, G., Bouvier, P., Ghosh, S., Rohrbach, A., Sanchez-Valle, C., 2013a. Single-crystal equation of state of phase D to lower mantle pressures and the effect of hydration on the buoyancy of deep subducted slabs. Journal of Geophysical Research-Solid Earth 118, 6124-6133.

Rosa, A.D., Sanchez-Valle, C., Ghosh, S., 2012. Elasticity of phase D and implication for the degree of hydration of deep subducted slabs. Geophys Res Lett 39, L06304.

Rosa, A.D., Sanchez-Valle, C., Nisr, C., Evans, S.R., Debord, R., Merkel, S., 2013b. Shear wave anisotropy in textured phase D and constraints on deep water recycling in subduction zones. Earth Planet Sc Lett 377, 13-22.

Rosa, A.D., Sanchez-Valle, C., Wang, J.Y., Saikia, A., 2015. Elasticity of superhydrous phase B, seismic anomalies in cold slabs and implications for deep water transport. Phys Earth Planet In 243, 30-43.

Rost, S., Garnero, E.J., Williams, Q.J.J.o.G.R.S.E., 2008. Seismic array detection of subducted oceanic crust in the lower mantle. 113.

Rudolph, M.L., Lekić, V., Lithgow-Bertelloni, C.J.S., 2015. Viscosity jump in Earth's mid-mantle. 350, 1349-1352.

Savage, B., 2012. Seismic constraints on the water flux delivered to the deep Earth by subduction. Geology 40, 235-238.

Schmandt, B., Jacobsen, S.D., Becker, T.W., Liu, Z., Dueker, K.G., 2014. Earth's interior. Dehydration melting at the top of the lower mantle. Science 344, 1265-1268.

Schumacher, L., Thomas, C., 2016. Detecting lower-mantle slabs beneath Asia and the Aleutians. Geophys J Int 205, 1512-1524.

Shieh, S.R., Duffy, T.S., Liu, Z.X., Ohtani, E., 2009. High-pressure infrared spectroscopy of the dense hydrous magnesium silicates phase D and phase E. Phys Earth Planet In 175, 106-114.

Shinmei, T., Irifune, T., Tsuchiya, J., Funakoshi, K.-I., 2008. Phase transition and compression behavior of phase D up to 46 GPa using multi-anvil apparatus with sintered diamond anvils. High Pressure Res 28, 363-373.

Shukla, G., Wentzcovitch, R.M., 2016. Spin crossover in $(Mg,Fe^{3+})(Si,Fe^{3+})O_3$ bridgmanite: Effects of disorder, iron concentration, and temperature. Phys Earth Planet In 260, 53-61.

Shukla, G., Wu, Z.Q., Hsu, H., Floris, A., Cococcioni, M., Wentzcovitch, R.M., 2015. Thermoelasticity of Fe^{2+}-bearing bridgmanite. Geophys Res Lett 42, 1741-1749.

Smyth, J.R., 1987. beta-Mg2 SiO4; a potential host for water in the mantle? Am Mineral 72, 1051-1055.

Song, Z., Wu, Z., Wang, W., Hao, S., Sun, D., 2022. Elasticity of Phase H Under the Mantle Temperatures and Pressures: Implications for Discontinuities and Water Transport in the Mid‐

Mantle. Journal of Geophysical Research: Solid Earth 127.

Thompson, E.C., Campbell, A.J., Tsuchiya, J., 2022. Calculated Elasticity of Al-Bearing Phase D. Minerals 12.

Tschauner, O., Huang, S., Greenberg, E., Prakapenka, V., Ma, C., Rossman, G., Shen, A., Zhang, D., Newville, M., Lanzirotti, A.J.S., 2018. Ice-VII inclusions in diamonds: Evidence for aqueous fluid in Earth's deep mantle. 359, 1136-1139.

Tsuchiya, J., Tsuchiya, T., 2008. Elastic properties of phase D ($MgSi_2O_6H_2$) under pressure: Ab initio investigation. Phys Earth Planet In 170, 215-220.

Tsuchiya, J., Tsuchiya, T., Tsuneyuki, S., 2005. First-principles study of hydrogen bond symmetrization of phase D under high pressure. Am Mineral 90, 44-49.

Wang, W., Zhang, H., Brodholt, J.P., Wu, Z.J.E., Letters, P.S., 2020. Elasticity of hydrous ringwoodite at mantle conditions: Implication for water distribution in the lowermost mantle transition zone. 116626.

Wang, W.Z., Walter, M.J., Peng, Y., Redfern, S., Wu, Z.Q., 2019. Constraining olivine abundance and water content of the mantle at the 410-km discontinuity from the elasticity of olivine and wadsleyite. Earth Planet Sc Lett 519, 1-11.

Waszek, L., Schmerr, N.C., Ballmer, M.D., 2018. Global observations of reflectors in the mid-mantle with implications for mantle structure and dynamics. Nat Commun 9, 385.

Wentzcovitch, R.M., Martins, J.L., Price, G.D., 1993. Ab initio molecular dynamics with variable cell shape: Application to $MgSiO_3$. Phys Rev Lett 70, 3947-3950.

Wu, X., Wu, Y., Lin, J.F., Liu, J., Mao, Z., Guo, X.Z., Yoshino, T., McCammon, C., Prakapenka, V.B., Xiao, Y.M., 2016. Two-stage spin transition of iron in FeAl-bearing phase D at lower mantle. Journal of Geophysical Research-Solid Earth 121, 6411-6420.

Wu, Z.Q., Wang, W.Z., 2016. First-principles calculations of elasticity of minerals at high temperature and pressure. Sci. China-Earth Sci. 59, 1107-1137.

Wu, Z.Q., Wentzcovitch, R.M., 2011. Quasiharmonic thermal elasticity of crystals: An analytical approach. Phys Rev B 83.

Xu, C., Gréaux, S., Inoue, T., Noda, M., Sun, W., Kuwahara, H., Higo, Y., 2020. Sound Velocities of Al‐Bearing Phase D up to 22 GPa and 1300 K. Geophys Res Lett 47.

Xu, C., Inoue, T., Kakizawa, S., Noda, M., Gao, J., 2021a. Effect of Al on the stability of dense hydrous magnesium silicate phases to the uppermost lower mantle: implications for water transportation into the deep mantle. Phys Chem Miner 48.

Xu, C., Li, Y., Inoue, T., Gréaux, S., Li, Q., Gao, J., Sun, F., Fang, L., 2021b. Elastic properties of Mg-phase D at high pressure. High Pressure Res 41, 233-246.

Xue, X., Kanzaki, M., Shatskiy, A., 2008. Dense hydrous magnesium silicates, phase D, and superhydrous B: New structural constraints from one- and two-dimensional 29Si and 1H NMR. Am Mineral 93, 1099-1111.

Yang, D.P., Wang, W.Z., Wu, Z.Q., 2017. Elasticity of superhydrous phase B at the mantle temperatures and pressures: Implications for 800 km discontinuity and water flow into the lower mantle. Journal of Geophysical Research-Solid Earth 122, 5026-5037.

Yang, H.X., Prewitt, C.T., Frost, D.J., 1997. Crystal structure of the dense hydrous magnesium silicate, phase D. Am Mineral 82, 651-654.

Yang, R., Wu, Z.Q., 2014. Elastic properties of stishovite and the $CaCl_2$-type silica at the mantle temperature and pressure: An ab initio investigation. Earth Planet Sc Lett 404, 14-21.

Yao, C., Wu, Z.Q., Zou, F., Sun, W.D., 2018. Thermodynamic and Elastic Properties of Magnesite at Mantle Conditions: First-Principles Calculations. Geochem Geophy Geosy 19, 2719-2731.

Zhang, Y., Fu, S., Wang, B., Lin, J.F., 2021. Elasticity of a Pseudoproper Ferroelastic Transition from Stishovite to Post-Stishovite at High Pressure. Phys Rev Lett 126, 025701.

Zou, F., Wu, Z.Q., Wang, W.Z., Wentzcovitch, R.M., 2018. An Extended Semianalytical Approach for Thermoelasticity of Monoclinic Crystals: Application to Diopside. Journal of Geophysical Research: Solid Earth 123, 7629-7643.